

An APN-Activatable Fluorescent Probe for Tracking Metastatic Cancer and Image-Guided Surgery via In-Situ Spraying

Haidong Li, Qichao Yao, Wen Sun, Kun Shao, Yang Lu, Jeewon Chung, Dayeh Kim, Jiangli Fan, Saran Long, Jianjun Du, Yueqing Li, Jingyun Wang, Juyoung Yoon, and Xiaojun Peng

J. Am. Chem. Soc., **Just Accepted Manuscript** • DOI: 10.1021/jacs.0c01365 • Publication Date (Web): 13 Mar 2020

Downloaded from pubs.acs.org on March 13, 2020

Just Accepted

“Just Accepted” manuscripts have been peer-reviewed and accepted for publication. They are posted online prior to technical editing, formatting for publication and author proofing. The American Chemical Society provides “Just Accepted” as a service to the research community to expedite the dissemination of scientific material as soon as possible after acceptance. “Just Accepted” manuscripts appear in full in PDF format accompanied by an HTML abstract. “Just Accepted” manuscripts have been fully peer reviewed, but should not be considered the official version of record. They are citable by the Digital Object Identifier (DOI®). “Just Accepted” is an optional service offered to authors. Therefore, the “Just Accepted” Web site may not include all articles that will be published in the journal. After a manuscript is technically edited and formatted, it will be removed from the “Just Accepted” Web site and published as an ASAP article. Note that technical editing may introduce minor changes to the manuscript text and/or graphics which could affect content, and all legal disclaimers and ethical guidelines that apply to the journal pertain. ACS cannot be held responsible for errors or consequences arising from the use of information contained in these “Just Accepted” manuscripts.

An APN-Activatable Fluorescent Probe for Tracking Metastatic Cancer and Image-Guided Surgery via In-Situ Spraying

Haidong Li,^{†,§} Qichao Yao,[†] Wen Sun,^{†,⊥} Kun Shao,^{†,⊥} Yang Lu,[†] Jeewon Chung,[§] Dayeh Kim,[§] Jiangli Fan,^{†,⊥} Saran Long,^{†,⊥} Jianjun Du,^{†,⊥} Yueqing Li,[‡] Jingyun Wang,^{||} Juyoung Yoon,^{*,§} and Xiaojun Peng^{*,†,⊥}

[†]State Key Laboratory of Fine Chemicals, Dalian University of Technology, 2 Linggong Road, Hi-tech Zone, Dalian 116024, P.R. China. *Email: (X. Peng) pengxj@dlut.edu.cn.

[‡]School of Pharmaceutical Science and Technology, Dalian University of Technology, 2 Linggong Road, Hi-tech Zone, Dalian 116024, P.R. China.

^{||}School of Life Science and Biotechnology, Dalian University of Technology, 2 Linggong Road, Hi-tech Zone, Dalian 116024, P.R. China.

[§]Department of Chemistry and Nanoscience, Ewha Womans University, Seoul 03760, Korea. *E-mail: (J. Yoon) jyoon@ewha.ac.kr.

[⊥]Shenzhen Research Institute, Dalian University of Technology, Nanshan District, Shenzhen 518057, P.R. China.

ABSTRACT: The recurrence of malignant tumors is mostly caused by incompleting surgical resection. Especially, it is difficult for surgeons to detect and accurately remove metastatic tumors by predominantly using visual examination and palpation owing to the lack of effective means to specifically distinguish the boundary range between normal and tumor tissues. Thus, the development of activated fluorescent probe with superior Tumor-to-Normal (T/N) tissue ratios is particularly urgent in clinics. In view of CD13/Aminopeptidase N (APN) regarded as a cancer-specific biomarker, mediating with progression, invasion and migration of malignant tumor, herein, we reported an APN-responsive fluorescent probe YH-APN, and demonstrated its application to distinguish cancer cells. Through *in-situ* spraying manner, fluorescent superior tumor-to-normal (T/N) tissue ratios (subcutaneous transplantation tumor: 13.86; hepatic metastasis: 4.42 and 6.25; splenic metastasis: 4.99) were achieved. More importantly, we have demonstrated the ability to image metastasis tumor tissue less than 1 mm in diameter, highlighting the potential for this probe to be used as a tool in surgical resection. This research may spur the use of enzyme-activatable fluorescent probes for the progress of tumor diagnosis and image-guided surgery (IGS).

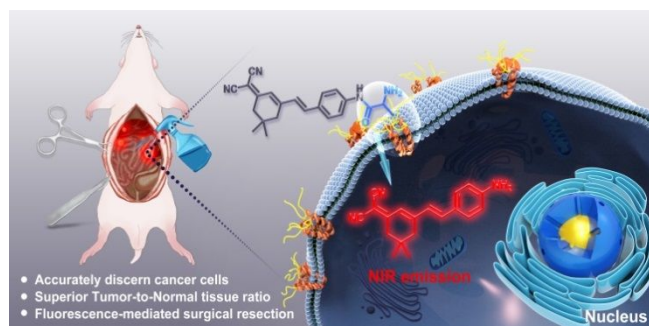
INTRODUCTION

Surgical removal of malignancies is still the first line of therapy, and in many cases provides the only curative treatment option.¹⁻³ During a surgery, visualizing the full extent of solid tumors comprising tumor borders, microscopic and metastatic lesions determines the outcome of the operation.⁴⁻⁵ Incomplete removal of tumor lesions will result in tumor recurrence,⁶⁻⁷ and thus the accurate detection of tumor in small sizes (less than 5 mm) is becoming even more important.⁸ Actually, the vast majority of tumors accompanied by tumor metastasis are clinically detected in the mid and late stages through conventional diagnostic approaches including magnetic resonance (MR)⁹⁻¹⁰, ultrasound (US)¹¹⁻¹² and X-ray computed tomography (CT)¹³⁻¹⁵ due to unsatisfactory resolution (more than 5 mm).⁶ In addition, these methods are also clinically inadequate because they are often

difficult to accurately distinguish the boundary between tiny tumor tissue and normal tissue, some nonpalpable and invisible foci (<2-3 mm) during surgery. In contrast, fluorescence imaging techniques are used in real-time monitoring of many physiological and pathological processes at the cellular and even molecular level.¹⁶⁻²⁶ Thus fluorescence imaging is a promising approach for tumor inspection during surgery.

In the last decade, efforts have focused on using fluorescent molecules or nanoparticles for visualizing tumors in animal models or human patients through their *in situ* spraying or intravenous injection.^{5, 27-31} These probes change the mode of surgical operations via visualizing the location of tumor lesions which are difficult or impossible to detect by human eyes.³² However, “always-on” probes, emitting fluorescence regardless of their interaction with the target tissues, result in

moderate or low tumor-to-normal tissue (T/N) ratio. Thus, fluorescence “always-on” probes lower the contrast between tumor and normal tissues. Activatable fluorescent molecules are promising for imaging *in vivo*.³³⁻⁴⁰ Target analytes specifically induce the fluorescence of molecules, allowing highly accurate imaging of tissues of interest.⁴¹⁻⁴⁴ Especially, activatable fluorescent molecules with emission in the therapeutic window (650-900 nm) are more suited for imaging-guided biomedical applications due to efficiently avoiding auto-fluorescence and improving tissue penetration.^{39, 45-49} Furthermore, tumor surgery practice also requires fast fluorescence response. Positive margins results of intraoperative frozen sections expose patients to the pain of re-operation to avoid the risk of recurrence.⁵⁰ Recently, some fluorescent probes activated by tumor enzymes have been reported, and the activatable processes take hours or more, unfavorable for a real-time imaging of tumors during a surgical practice.⁵¹⁻⁵³ Therefore, the effective strategy for image-guided surgery with a high T/N ratio and fast fluorescence response is particularly urgent for visualizing the contrast between tumor and normal tissues and thus enables precisely removal of tumors in small sizes during intraoperative applications.



Scheme 1. Schematic illustration demonstrating the recognition mechanism of YH-APN as the activatable probe towards APN and its biological applications.

To address the aforementioned challenge, herein, we reported an activatable fluorescent molecule YH-APN to improve imaging-guided tumor surgery *via* tracking a tumor-specific enzyme, CD13/aminopeptidase N (APN, EC 3.4.11.2).⁵⁴⁻⁵⁶ APN is one of the zinc metallopeptidases anchoring on the extracellular membrane, and also regarded as a biomarker associated with the onset, invasion, angiogenesis and migration of cancer cells.⁵⁷⁻⁵⁸ We found that in response to APN, the emission of YH-APN was rapidly activated through one step enzymatic reaction. In addition, YH-APN was capable of accurately monitoring APN activity in cancer cells with a high signal-to-noise ratio due to its ultra-sensitivity and excellent selectivity. Furthermore, YH-APN was able to do real-time imaging of solid tumors with superior tumor-to-normal (T/N) tissue ratio (13.86) through *in situ* spraying. More importantly, metastatic lesions with less than 1 mm were precisely removed under fluorescence

guidance. These findings of fluorescence-mediated tumor surgery through *in situ* spraying APN-activatable molecules hold potential for clinical applications.

RESULTS AND DISCUSSION

Synthesis and spectroscopic characteristics. The enzyme-activatable fluorescent probe YH-APN was synthesized *via* a five-step route (Scheme S1). The intermediates and YH-APN were fully characterized using nuclear magnetic resonance (¹H, ¹³C NMR) and high resolution mass spectrum (ESI-HRMS) in supporting information (Figure S32-34). YH-APN was composed of two moieties: a dicyanoisophorone fluorophore as the fluorescence reporting unit, and an L-alanine as the recognition site for APN. Once interacting with APN, the structure of YH-APN was transformed into intermediate 5, releasing fluorescence emission of 650 nm which was ascribed to the modulation of the conjugated π -electron system of dicyanoisophorone dyes.

The UV-Vis absorption titration spectral of YH-APN in PBS buffer solution (0.01 M, pH = 7.4) was displayed in Figure S1a. It clearly showed that YH-APN can be well dissolved in aqueous solution with a favorable solubility up to 100 μ M (Figure S1b). The optical responses towards APN were carried out in PBS buffer (0.01 M, pH = 7.4). In response to 100 ng/mL APN, obvious red-shift of absorption spectra of YH-APN (10 μ M) ranging from 407 nm to 445 nm were observed, along with color changes of solution (Figure S2 and S3). The fluorescence profiles of YH-APN (10 μ M) also experienced significant enhancement in response to APN, which was ascribed to the precise cutting of amide bond to emit strong fluorescence, further convincing the enzymatic reaction (Figure 1a). The fluorescence intensity centered at 650 nm was linearly proportional to APN concentrations (1-9 ng/mL). The detection limit was calculated to be 0.13 ng/mL (Figure 1b), better than previous 0.8 ng/mL.⁵⁶ Such a low detection limit enables the ultra-sensitivity of YH-APN to APN *in vitro*.

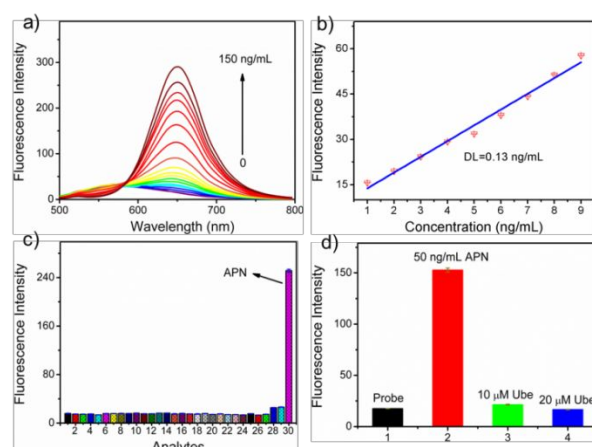


Figure 1. a) Fluorescence spectrometric titration experiments. b) The linear functional relationship between the fluorescence intensity of 650 nm and low concentration APN.

c) Selectivity of YH-APN towards different analytes in PBS buffer solution. Except for special statement, all other concentrations were 500 μM . Insert 1: blank, 2: Na^+ , 3: K^+ , 4: Ca^{2+} , 5: Ni^{2+} , 6: Mg^{2+} , 7: NH_4^+ , 8: F^- , 9: Cl^- , 10: Br^- , 11: I^- , 12: CH_3COO^- , 13: HCO_3^- , 14: CO_3^{2-} , 15: S^{2-} , 16: HPO_4^{2-} , 17: NO_3^- , 18: SO_4^{2-} , 19: SCN^- , 20: NO_2^- , 21: Glutathione, 22: Cysteine, 23: Homocysteine, 24: Ascorbic acid, 25: NO , 26: H_2O_2 (100 μM); 27: nitroreductase (10 $\mu\text{g}/\text{mL}$); 28 transglutaminase (60 mU/mL); 29: γ -GGT (300 ng/mL) 30: APN (100 ng/mL). d) Inhibition characterization of APN activity with Ubenimex (Ube).

In addition, a large Stokes shift of 205 nm could avoid self-quenching and also greatly improve the accuracy of detection (Figure S4). The specificity of recognition is one of the vital indicators to investigate the usability of the probe. Interestingly, only APN could cause a dramatic change in fluorescence behavior under the identical condition, which indicated that YH-APN could serve as a potential tool for specifically detecting APN activity in complex biological systems (Figure 1c and S5). Subsequently, the time response experiment of YH-APN reacting with APN (40 ng/mL) was performed at 37 $^\circ\text{C}$ in aqueous solution. A very strong fluorescence intensity of 650 nm could be detected after half an hour (Figure S6). In contrast, in the absence of APN, there was no distinct changes up to 400 min in the spectral of absorption (Figure S7, S8 and S9), suggesting good stability of YH-APN in the physiological environment. The effect of analysis conditions including temperature and pH were further explored. As displayed in Figure S10 and S11, YH-APN demonstrated excellent stability under different temperatures (25-50 $^\circ\text{C}$) and pH values (4.75-10.27) in PBS buffer solution. After adding 50 ng/mL APN, the optimum value for increased fluorescence intensity was at 37 $^\circ\text{C}$ and $\text{pH} = 7.4$, which inferred that YH-APN was capable of efficiently identifying endogenous APN under physiological conditions.

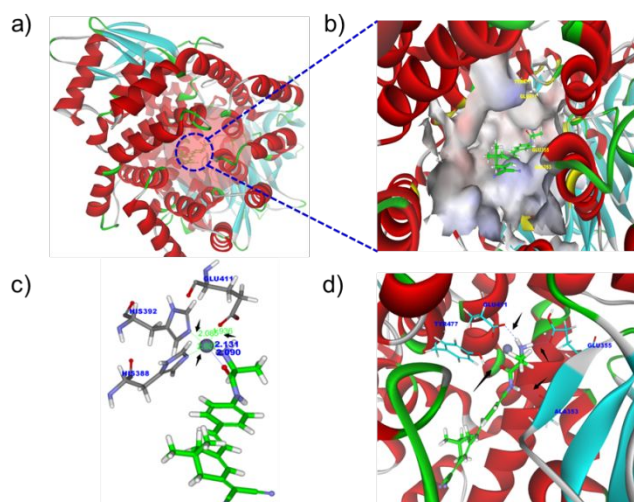


Figure 2. a) Stereo image of human APN with binding location (red transparent sphere). b) YH-APN reached coordination center of zinc ion through wide-opening hydrophobic cavity. c) The lengths of coordination bond between YH-APN and APN. d) Hydrogen bonds between YH-APN and residues amino acid Tyr477, Glu411, Glu355, and Ala353 in APN.

Response mechanism. The specific response of YH-APN to APN encouraged us to investigate the interaction between YH-APN and APN. Docking calculations based on Discovery Studio 2.5 platform were carried out for this purpose. The crystal structure of human APN from PDB database was selected as the research model. YH-APN tends to approach the coordination center of zinc ion due to matching the hydrophobic cavity of the enzyme (Figure 2a and 2b). Lengths of the coordination bond between YH-APN and APN was 2.090 \AA (Zn-O, Figure S12) and 2.131 \AA (Zn-N, Figure S12), infinitely close to its inherent coordinate distance with amino acid residues (2.027 \AA , 2.085 \AA , and 1.936 \AA , Figure 2c). In addition, the presence of hydrogen bonds between YH-APN and amino acid residues Tyr477, Glu411, Glu355, and Ala353 allowed it to firmly anchor in the specific cavity of APN (Figure 2d). With the help of the catalytic system centering on zinc ions, YH-APN was converted into intermediate 5 with the exposed amino group which was a strong electron donor, resulting in the increasement fluorescence around 650 nm. A major peak (m/z) at 290.1655 was found in high resolution mass spectra (Figure S13) of catalytic products, which was consistent with the positive ion (H^+) mode of intermediate 5 (calcd. 290.1652 for $[\text{M}+\text{H}]^+$). The fluorescence intensity of YH-APN was reduced by 86.2% and 89.5% (Figure 1d and S14) with the presence of 10 μM and 20 μM Ubenimex (Ube, APN inhibitor)⁵⁵ compared to the control group without Ube, further verifying the reaction mechanism (Scheme 1). Besides, the normalization excitation and emission profiles of YH-APN (10 μM) with 150 ng/mL APN at 37 $^\circ\text{C}$ in PBS buffer solution (Figure S15) were perfectly coincident with the profiles of intermediate 5 (Figure S16). These results clearly demonstrated that YH-APN could be identified by APN, which led to the uncaging of the amino group and emitted fluorescence.

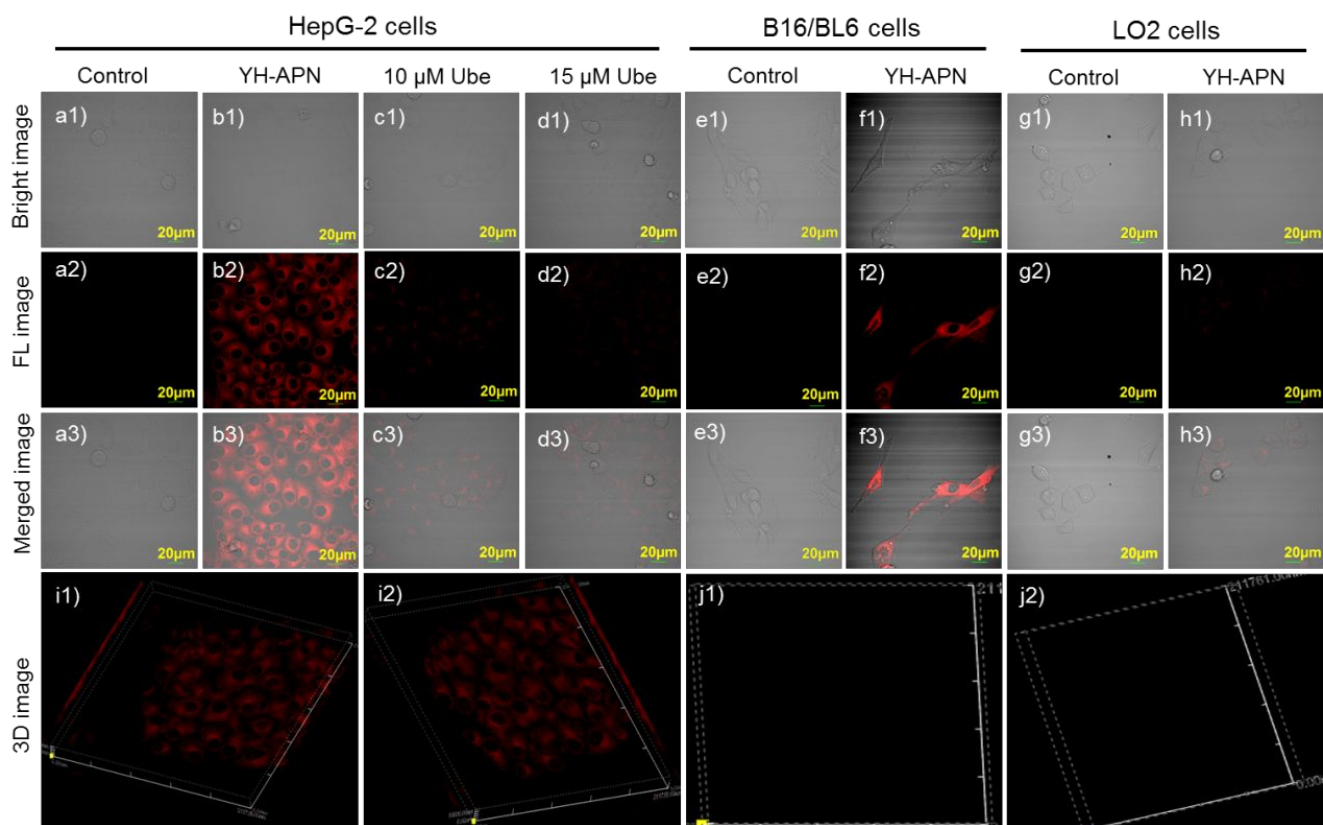


Figure 3. Fluorescence imaging of HepG-2, B16/BL6, LO2 cells treated with 5 μM probe YH-APN at 37 $^{\circ}\text{C}$ for 30 min. a-d) HepG-2 cells: a1-a3) control group; b1-b3) incubated with 5 μM probe YH-APN; c1-c3) pre-treated with 10 μM Ube, then incubated with 5 μM probe YH-APN; d1-d3) pre-treated with 15 μM Ube, then incubated with 5 μM probe YH-APN. e-f) B16/BL6 cells: e1-e3) control group; f1-f3) incubated with 5 μM probe YH-APN. g-h) LO2 cells: g1-g3) control group; h1-h3) incubated with 5 μM probe YH-APN. i) 3D fluorescence imaging of HepG-2 cells; j) 3D fluorescence imaging of LO2 cells. $\lambda_{\text{ex}} = 488 \text{ nm}$ and $\lambda_{\text{em}} = 655\text{-}755 \text{ nm}$. Scale bar = 20 μm .

Response speed and Selectivity Fluorescence imaging of APN-overexpression cancer cells.

Biocompatibility of probes is a prerequisite to cell and *in vivo* imaging. Thus, the biocompatibility of YH-APN was firstly investigated. Cytotoxicity of YH-APN was determined through conventional 5-diphenyltetrazolium bromide (MTT) assays. As shown in Figure S17, YH-APN was not cytotoxic to cells, laying a good foundation for the tracking of endogenous APN in living cells and *in vivo*.

The availability of YH-APN for monitoring endogenous APN in living cells was investigated. The apparent fluorescence signal of 655-755 nm (Figure 3b2) was collected from HepG-2 cells (hepatoma carcinoma cells) after incubation with YH-APN (5 μM) for 30 min, which was attributed to the overexpression APN on the surface of malignant tumor cells.⁵⁷⁻⁵⁸ Furthermore, the fluorescence intensity steadily increased with time (0, 30 and 60 min, Figure S18). Dose-dependent effect of probe YH-APN was also studied in HepG-2 cells with various concentrations (0, 5, 10 and 15 μM , Figure S19), indicating

that YH-APN was efficiently catalyzed by APN. HepG-2 cells were pre-treated with Ube (a specific inhibitor of APN) for 1 h, followed by adding 5 μM YH-APN for another 30 min. Almost no fluorescence (Figure 3c2 and 3d2) was detected, because Ube occupies the catalytic site, and inhibits the enzymatic hydrolytic substrate. The result confirmed that the fluorescence signal was indeed induced by endogenous APN catalysis. Moreover, obvious fluorescence emission from B16/BL6 cells (mouse melanoma cells)⁵⁵ was also detected because APN was overexpressed in B16/BL6 cells (Figure 3f2). By comparison, normal human liver cells (LO2) and African green monkey kidney fibroblasts cells (COS-7) were chosen as the negative groups due to their low-level APN expression. As expected, no obvious fluorescence was observed from LO2 and COS-7 cells under the identical conditions (Figure 3h2 and S20), further indicating that the overexpression of APN plays a vital role in inducing the fluorescence signals of YH-APN.

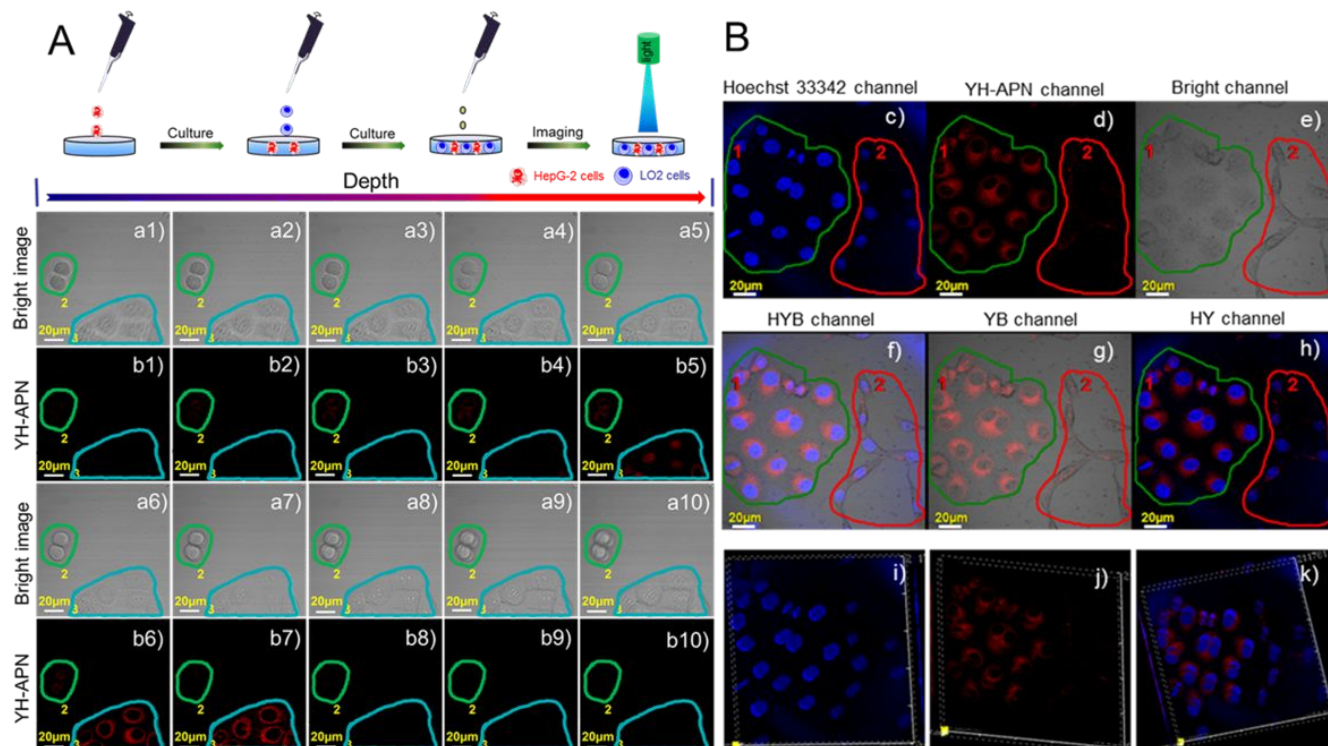


Figure 4. Fluorescence imaging of mixed culture cells treated with YH-APN probe. a1–b10) Deep scan imaging of mixed cultivation cells of HepG-2 (cyan region) and LO2 (green region). c–h) Intensity projection over z-axis of the different channel of HepG-2 (green region) and COS-7 (red region). (i–k) Reconstructed 3D imaging of mixed cultivation cells. $\lambda_{ex} = 488$ nm and $\lambda_{em} = 655\text{--}755$ nm. Scale bar = 20 μm .

Three-dimensional imaging provides a more accurate view of the whole. Cancer cells (HepG-2 cells and B16/BL6 cells) were exactly distinguished from normal cells (LO2 cells and COS-7 cells) through 3D imaging relying on different amounts of endogenous APN on their cell surface (Figure 3i, 3j, S21 and S22). Subsequently, high throughput analysis for demonstrating the ability of YH-APN to distinguish cancer cells was conducted on LO2 cells and HepG-2 cells *via* flow cytometry (FCM). The fluorescence intensity of cancer cells and normal cells could be obviously distinguished after incubating cells with YH-APN (7.5 μM) for 30 min (Figure S23a3 and S23b5). However, the fluorescence intensity of HepG-2 cells was essentially suppressed when cells were pre-incubated with Ube (10 μM) for 1 h (Figure S23a2). Overall, YH-APN was capable of differentiating cancer cells from normal cells *via* 2D&3D imaging and flow cytometry.

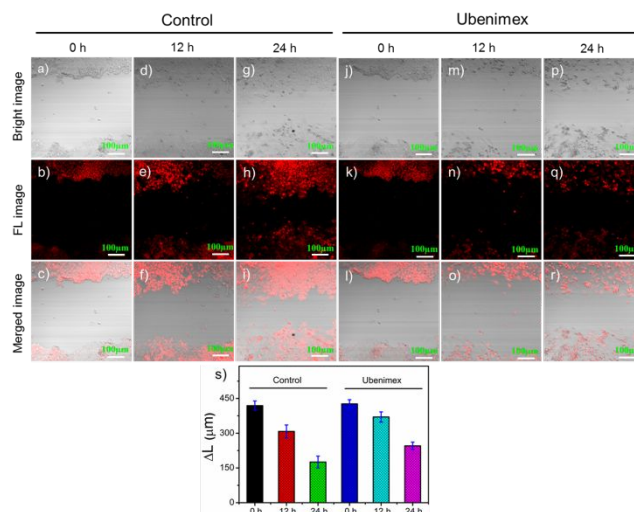


Figure 5. Migration characterization of malignant tumor cells. a–i): HepG-2 cells treated with YH-APN; j–r) HepG-2 cells pre-incubated with 100 μM Ube, then treated with YH-APN; s) the distance of scratch collected from b, d, g, j, m, and p, respectively. $\lambda_{ex} = 488$ nm, $\lambda_{em} = 655\text{--}755$ nm. Scale bar = 100 μm .

In fact, it is still inadequate to identify cancer cells from the separated culture of cells for early detection of tumors, because the early position of the tumor is where normal cells and cancer cells coexist.⁵⁹ Thus, the ability of YH-APN to identify cancer cells in the mixed cultivation

of cells is of great importance for the early diagnosis of tumors. The early neoplastic simulating experiments were carried out to verify the above functionality. HepG-2 cells were planted and cultured for 24 h. Subsequently, LO2 cells were cultured on the same confocal dish for another 24 h (Figure 4). The mixed cultivation cells of HepG-2 and LO2 were then treated with YH-APN ($5\ \mu\text{M}$, $37\ ^\circ\text{C}$) for 30 min, followed by deep scan imaging of cells *via* $3\ \mu\text{m}$ as a step along the *z* axis. Normal and cancer cells can be distinguished by cell morphology (Figure 4a1-a10). The remarkable fluorescence signal of 655-755 nm was collected from the cyan region (HepG-2 cells, Figure 4b7) compared to the green region (LO2 cells) (Figure 4, b1-b10), which was attributed to overexpression of APN in HepG-2 cells. Besides, tumor cells (Figure 4h, green region) could be selectively lighten up depending on dual mark (APN activity labelled by YH-APN; Nucleic acid labelled by commercial Hoechst 33342), which was further confirmed by fluorescence imaging of mixed culture cells of HepG-2 and COS-7 (Figure 4c-h) as well as corresponding 3D imaging (Figure 4i-k). The above experimental results indicated that YH-APN may have the potential for the discrimination of APN-related cancer cells from normal cells.

The invasion and migration is the most basic biological feature of malignant tumors, which is the main reason for cancer metastasis. Current researches have demonstrated that Aminopeptidases N (APN) plays a key role in regulating the migration of malignant tumor cells.⁵⁷⁻⁵⁸ Thus, the migration of tumor cells was expected to be determined *via* fluorescence imaging of APN. The tumor cell migration was established based on cell scratch. With the addition of Ube, the appearance of shrinkage was found in the cell morphology of HepG-2 (Figure 5m and 5p) compared to the control group (Figure 5d and 5g). The migration distance of HepG-2 cells incubated with $100\ \mu\text{M}$ Ube was apparently prevented because of APN activity inhibited on the cell surface (Figure 5n and 5q). As is seen in Figure 5s, the migration ratios of Ube treatment and control group of cells were 13.15%, 26.56% (12 h) and 42.49%, 58.13% (24 h), respectively. The above results clearly demonstrated that invasion of tumors can be imaged by HY-APN, which is important for fluorescence imaging of microscopic and metastatic tumor lesions.

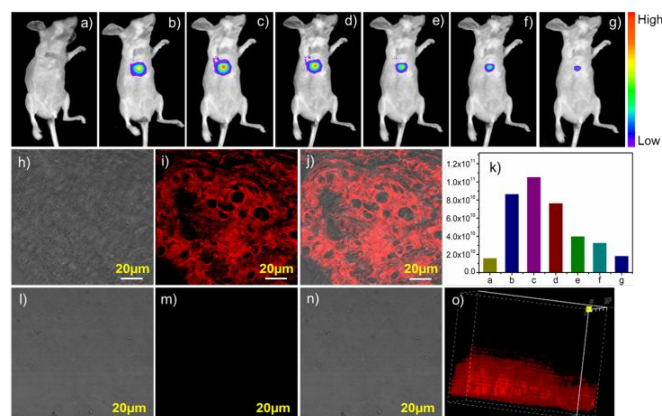


Figure 6. Imaging of endogenous APN activity in bare BABL/c mice bearing HepG-2 xenograft tumor and various tissues. Time-dependent fluorescence photographs for mouse intratumoral injection with probe YH-APN ($50\ \mu\text{M}$, $50\ \mu\text{L}$): a) 0 min; b) 20 min; c) 50 min; d) 70 min; e) 100 min; f) 120 min; g) 150 min. k) Average ph/s was collected from the tumor site as the corresponding time. h-j) imaging of tumor tissue; l-n) imaging of normal tissue, $\lambda_{\text{ex}} = 488\ \text{nm}$, $\lambda_{\text{em}} = 655\text{-}755\ \text{nm}$. Scale bar = $20\ \mu\text{m}$. Fluorescence imaging of mouse was gathered with an excitation filter of $475\ \text{nm}$ (fwhm $20\ \text{nm}$) and an emission filter of $655\ \text{nm}$ (fwhm $20\ \text{nm}$). o) 3D imaging of tumor tissue with two-photon excitation of $800\ \text{nm}$ and emission of $575\text{-}630\ \text{nm}$.

Imaging of endogenous APN in tissues and *in vivo*.

Inspired by the desired activatable emission in responsive to APN, the capability of YH-APN for visualization of endogenous APN *in vivo* was then investigated. HepG-2 cells (1×10^6 cells) owing to overexpression APN was transplanted around the axilla of the right limb of female nude BABL/c mice to establish the animal research model. All the animal procedures were performed in accordance with the Guidelines for Care and Use of Laboratory Animals of Dalian Medical University and experiments were approved by Dalian Medical University Animal Care and Use Committee. Upon tumor formation, the mice were pre-anaesthetized, and *in vivo* imaging was performed on a small animal imaging system. Distinct fluorescence ($645\text{-}665\ \text{nm}$) was obtained from the tumor site after directly injected with YH-APN ($50\ \mu\text{M}$, $50\ \mu\text{L}$) 20 min later due to rapid cleavage of amide bond by APN (Figure 6b). The fluorescence can be restored up to 70 min with a high tumor-to-normal tissue (T/N) ratio (Figure 6a-6d). As mentioned above, the histopathological biopsy is required during current tumor surgery, which is trapped in the time-consuming of sample preparation and complex operation. Rapid, convenient, simple and correct are thus the requirements for further tumor diagnosis. To demonstrate the efficiency and reliability of the probe in identifying tumor tissues from normal tissues, imaging of various tissue sections was conducted on confocal fluorescence microscopy. Tissue slices of $20\ \mu\text{m}$ were prepared by freezing microtome were incubated with YH-APN ($5\ \mu\text{M}$) for 30 min under room temperature.

Compared to normal liver tissue (Figure 6l-6m), the remarkable fluorescence signal (Figure 6h-6j) was gathered from hepatocellular carcinoma tissue. Correspondingly, the 3D reconstruction imaging also demonstrated the reliability of YH-APN for imaging APN in tissue level (Figure 6o, S24, and S25).

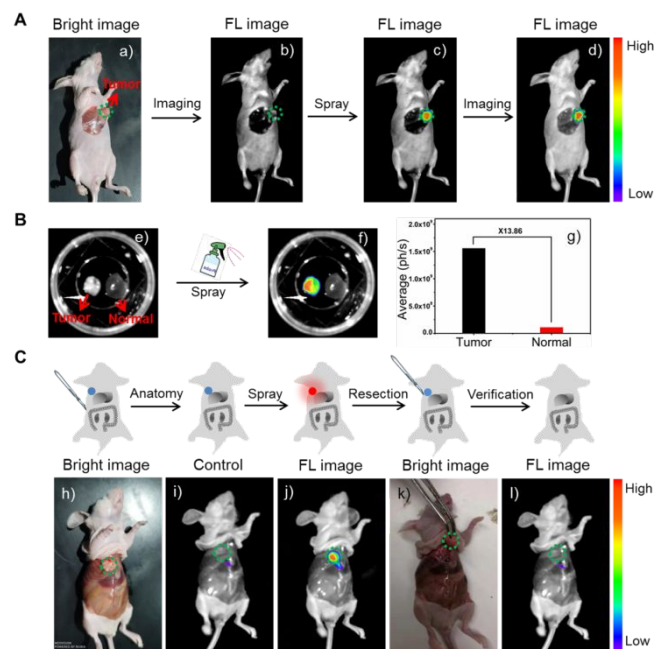


Figure 7. Image-guided resection by spraying YH-APN in bare BALB/c mice bearing HepG-2 xenograft tumor. A) *in-situ* spraying imaging *in vivo*: a) bright image; b) fluorescence image; c) spraying YH-APN for 30 min, then fluorescence image; d) based on c), the slipped effusion removed and fluorescence image. B) *in vitro* imaging of liver tissue and normal liver tissue (e and f) through spraying probe YH-APN for 30 min, g) statistical fluorescence intensities. C) image-guided resection by spraying probe YH-APN: h) bright image; i) fluorescence image; j) spraying YH-APN for 30 min, then fluorescence image; k) surgical removal of tumor; l) based on k), respraying YH-APN for 30 min, and fluorescence image. Fluorescence imaging of mouse was gathered with an excitation filter of 475 nm (fwhm 20 nm) and an emission filter of 655 nm (fwhm 20 nm).

Image-guided resection by spraying YH-APN. In order to gain precise image-guided resection for the tumor, YH-APN can be utilized to visualize the full outline of tumors. Initially, we demonstrated that the tumor could be accurately lit up *in situ* by simply spraying YH-APN (Figure 7c and 7d). In contrast, no fluorescence signal was obtained from the control group (Figure 7b). Additionally, *in vitro* liver cancer tissue and normal tissue could also be effectively distinguished *via in situ* spraying of YH-APN (Figure 7e and 7f). The T/N ratio of 13.86 was gathered and kept at least for 2 h, facilitating to accurately identify cancerous tissues (Figure 7g). Based on the above results, obvious fluorescent tissue (Figure 7j) from the mouse was removed with a scalpel (Figure 7k). No

fluorescence signal was collected (Figure 7l) when the probe was sprayed at the original location, which is in accordance with the control group (Figure 7i). These *in vivo* imaging results signified that the tumor was removed. Therefore, YH-APN may serve as a powerful contrast probe to assist accurate tumor resection in the clinical field.

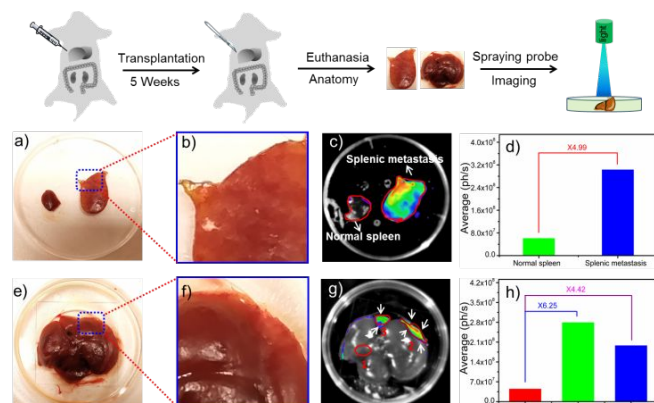


Figure 8. Imaging of metastatic cancer through spraying YH-APN in BALB/c mice bearing 4T1 xenograft tumor (s.c. close to mammary gland for 5 weeks). Splenic metastasis: a) bright image (left side: normal spleen; right side: splenic metastasis); b) detail with enlarged scale; c) spraying YH-APN for 30 min, then fluorescence image; d) statistical fluorescence intensities. Hepatic metastases: e) bright image; f) detail with enlarged scale; g) spraying YH-APN for 30 min, then fluorescence image; h) statistical fluorescence intensities. Fluorescence imaging of mouse was gathered with an excitation filter of 475 nm (fwhm 20 nm) and an emission filter of 655 nm (fwhm 20 nm).

Imaging of metastatic cancer. The unsuccessful removal of micro-metastatic lesions during surgery always results in tumor metastasis, which is the key reason for the dissatisfactory overall survival of patients with malignant tumors. To further investigate the clinical application of YH-APN, we constructed a metastatic tumor model in BALB/c mice bearing 4T1 xenograft tumor. After sacrifice, spleen and liver samples were discreetly taken out from mice, and then washed with PBS buffer for three times. Compared to the normal spleen (Figure 8a, left side), metastatic spleen (Figure 8a, right side) became markedly swollen. After spraying the agent, the tissue of splenic metastasis showed apparent fluorescence. However, no fluorescence was observed from normal spleen (Figure 8c). A high T/N tissue ratio of 4.99 was gathered (Figure 8d). In addition, we also used this method in tissue with liver metastasis (Stage II, multiple metastases involving less than 25% of hepatic parenchyma)⁶⁰⁻⁶¹ (Figure 8e and 8f). Metastatic lesions with less than 1 mm in diameter could also be clearly imaged (Figure 8g), which is superior to the traditional diagnostic methods in clinical practice. Thus, T/N tissue ratios (Figure 8h) of 4.42 (Figure 8g, ROI₃/ROI₁) and 6.25 (Figure 8g, ROI₂/ROI₁) were favorable for the accurate

resection of micro-metastatic tumors. These experiments suggested that YH-APN could track metastatic tumor lesions within organs by *in-situ* spraying manner, which would inevitably promote the accuracy of tumor resection.

CONCLUSION

In summary, we presented an enzyme-activatable fluorescent probe YH-APN for guiding surgical resection via monitoring endogenous APN activity. Spectral analysis, theoretical simulation, and high-resolution mass spectrum provided clear proof for the recognition of probe towards APN. YH-APN demonstrated ultrasensitive detection limit to APN (DL 0.13 ng/mL) with excellent selectivity and favorable biocompatibility. Tumor cells (HepG-2 and B16/BL6 cells) were accurately lighted-up by YH-APN in the separated and co-culture system through 2D&3D imaging, showing the level of single-cell recognition. Notably, high tumor-to-normal (T/N) tissue ratios were firstly observed in *in-vivo* tests which may enable future applications in image-guided surgery. These results elucidated that YH-APN can be used as a vital research tool, and has potential applications in diagnosis of metastatic disease in healthcare.

ASSOCIATED CONTENT

Supporting Information

More compounds characterizations, experimental procedures, related spectrum and others supplementary materials are available in Supporting Information. This material is available free of charge on the ACS publications website.

AUTHOR INFORMATION

Corresponding Author

*jyoon@ewha.ac.kr; Tel/Fax: +82-2-3277-2400/2385.

*pengxj@dlut.edu.cn; Tel/Fax: +86 -411- 84986306.

Notes

The authors declare no competing financial interests.

ACKNOWLEDGEMENTS

This work was supported by National Science Foundation of China (21421005, 21576037, 21808028), the NSFC-Liaoning United Fund (U1608222, U1908202), and National Creative Research Initiative programs of the National Research Foundation of Korea (NRF) funded by the Korean government (MSIP) (no. 2012R1A3A2048814).

REFERENCES

1. Wilson, S. M.; Adson, M. A., Surgical treatment of hepatic metastases from colorectal cancers. *Arch. Surg.* **1976**, *111*, 330-334.
2. Markhede, G.; Angervall, L.; Stener, B., A multivariate analysis of the prognosis after surgical treatment of malignant soft-tissue tumors. *Cancer* **1982**, *49*, 1721-1733.
3. Morgan, W. R.; Zincke, H., Progression and survival after renal-conserving surgery for renal cell carcinoma: experience in 104 patients and extended followup. *J. Urology* **1990**, *144*, 852-857.
4. Urano, Y.; Sakabe, M.; Kosaka, N.; Ogawa, M.; Mitsunaga, M.; Asanuma, D.; Kamiya, M.; Young, M. R.; Nagano, T.; Choyke, P. L.; Kobayashi, H., Rapid cancer detection by topically spraying a γ -glutamyltranspeptidase-activated fluorescent probe. *Sci. Transl. Med.* **2011**, *3*, 110ra119.
5. Wang, P.; Fan, Y.; Lu, L.; Liu, L.; Fan, L.; Zhao, M.; Xie, Y.; Xu, C.; Zhang, F., NIR-II nanoprobe in-vivo assembly to improve image-guided surgery for metastatic ovarian cancer. *Nat. Commun.* **2018**, *9*, 2898.
6. El-Kashlan, H. K.; Zeitoun, H.; Arts, H. A.; Hoff, J. T.; Telian, S. A., Recurrence of acoustic neuroma after incomplete resection. *Otol. Neurotol.* **2000**, *21*, 389-392.
7. Sarmiento, J. M.; Heywood, G.; Rubin, J.; Ilstrup, D. M.; Nagorney, D. M.; Que, F. G., Surgical treatment of neuroendocrine metastases to the liver: a plea for resection to increase survival. *J. Am. Coll. Surgeons* **2003**, *197*, 29-37.
8. Park, Y.; Ryu, Y.-M.; Wang, T.; Jung, Y.; Kim, S.; Hwang, S.; Park, J.; Bae, D.-J.; Kim, J.; Moon, H.; Lim, H.-S.; Kim, S.-Y.; Chung, E.; Kim, K. H.; Kim, S.; Myung, S.-J., Colorectal cancer diagnosis using enzyme-sensitive ratiometric fluorescence dye and antibody-quantum dot conjugates for multiplexed detection. *Adv. Funct. Mater.* **2018**, *28*, 1703450.
9. Ma, X.; Tao, H.; Yang, K.; Feng, L.; Cheng, L.; Shi, X.; Li, Y.; Guo, L.; Liu, Z., A functionalized graphene oxide-iron oxide nanocomposite for magnetically targeted drug delivery, photothermal therapy, and magnetic resonance imaging. *Nano Res.* **2012**, *5*, 199-212.
10. Yang, K.; Hu, L.; Ma, X.; Ye, S.; Cheng, L.; Shi, X.; Li, C.; Li, Y.; Liu, Z., Multimodal imaging guided photothermal therapy using functionalized graphene nanosheets anchored with magnetic nanoparticles. *Adv. Mater.* **2012**, *24*, 1868-1872.
11. Lee, C. H.; Dershaw, D. D.; Kopans, D.; Evans, P.; Monsees, B.; Monticciolo, D.; Brenner, R. J.; Bassett, L.; Berg, W.; Feig, S.; Hendrick, E.; Mendelson, E.; D'Orsi, C.; Sickles, E.; Burhenne, L. W., Breast cancer screening with imaging: recommendations from the society of breast imaging and the ACR on the use of mammography, breast MRI, breast ultrasound, and other technologies for the detection of clinically occult breast cancer. *J. Am. Coll. Radiol.* **2010**, *7*, 18-27.
12. Mallidi, S.; Luke, G. P.; Emelianov, S., Photoacoustic imaging in cancer detection, diagnosis, and treatment guidance. *Trends Biotechnol.* **2011**, *29*, 213-221.
13. Wang, H.; Zheng, L.; Peng, C.; Guo, R.; Shen, M.; Shi, X.; Zhang, G., Computed tomography imaging of cancer cells using acetylated dendrimer-entrapped gold nanoparticles. *Biomaterials* **2011**, *32*, 2979-2988.
14. Kinsella, J. M.; Jimenez, R. E.; Karmali, P. P.; Rush, A. M.; Kotamraju, V. R.; Gianneschi, N. C.; Ruoslahti, E.; Stupack, D.; Sailor, M. J., X-ray computed tomography imaging of breast cancer by using targeted peptide-labeled bismuth sulfide nanoparticles. *Angew. Chem. Int. Ed.* **2011**, *50*,

12308-12311.

15. Rabin, O.; Perez, J. M.; Grimm, J.; Wojtkiewicz, G.; Weissleder, R., An X-ray computed tomography imaging agent based on long-circulating bismuth sulphide nanoparticles. *Nat. Mater.* **2006**, *5*, 118.
16. Chen, Z.; Mu, X.; Han, Z.; Yang, S.; Guo, Z.; Bai, Y.; He, W., An optical/photoacoustic dual-modality probe: ratiometric in/ex vivo imaging for stimulated H₂S upregulation in mice. *J. Am. Chem. Soc.* **2019**, *141*, 17973-17977.
17. Kim, E.-J.; Kumar, R.; Sharma, A.; Yoon, B.; Kim, H. M.; Lee, H.; Hong, K. S.; Kim, J. S., In vivo imaging of β -galactosidase stimulated activity in hepatocellular carcinoma using ligand-targeted fluorescent probe. *Biomaterials* **2017**, *122*, 83-90.
18. Liu, H.-W.; Chen, L.; Xu, C.; Li, Z.; Zhang, H.; Zhang, X.-B.; Tan, W., Recent progresses in small-molecule enzymatic fluorescent probes for cancer imaging. *Chem. Soc. Rev.* **2018**, *47*, 7140-7180.
19. Li, H.; Yao, Q.; Xu, F.; Li, Y.; Kim, D.; Chung, J.; Baek, G.; Wu, X.; Hillman, P. F.; Lee, E. Y.; Ge, H.; Fan, J.; Wang, J.; Nam, S.-J.; Peng, X.; Yoon, J., An activatable AIEgen probe for high-fidelity monitoring of overexpressed tumor enzyme activity and its application to surgical tumor excision. *Angew. Chem. Int. Ed.*, **2020**, DOI: 10.1002/anie.202001675.
20. Zhang, J.; Chai, X.; He, X.-P.; Kim, H.-J.; Yoon, J.; Tian, H., Fluorogenic probes for disease-relevant enzymes. *Chem. Soc. Rev.* **2019**, *48*, 683-722.
21. Sedgwick, A. C.; Dou, W.-T.; Jiao, J.-B.; Wu, L.; Williams, G. T.; Jenkins, A. T. A.; Bull, S. D.; Sessler, J. L.; He, X.-P.; James, T. D., An ESIPT Probe for the Ratiometric Imaging of Peroxynitrite Facilitated by Binding to A β -Aggregates. *J. Am. Chem. Soc.* **2018**, *140*, 14267-14271.
22. Wu, D.; Sedgwick, A. C.; Gunnlaugsson, T.; Akkaya, E. U.; Yoon, J.; James, T. D., Fluorescent chemosensors: the past, present and future. *Chem. Soc. Rev.* **2017**, *46*, 7105-7123.
23. Murfin, L. C.; Weber, M.; Park, S.J.; Kim, W. T.; Lopez-Alled, C. M.; McMullin, C. L.; Pradaux-Caggiano, F.; Lyall, C. L.; Kociok-Köhn, G.; Wenk, J.; Bull, S. D.; Yoon, J.; Kim, H. M.; James, T. D.; Lewis, S. M., Azulene-derived fluorescent probe for bioimaging: detection of reactive oxygen and nitrogen species by two-photon microscopy. *J. Am. Chem. Soc.* **2019**, *141*, 19389-19396.
24. Gu, K.; Liu, Y.; Guo, Z.; Lian, C.; Yan, C.; Shi, P.; Tian, H.; Zhu, W. H., In situ ratiometric quantitative tracing of intracellular leucine aminopeptidase activity via an activatable near-infrared fluorescent probe. *ACS Appl. Mater. Interfaces* **2016**, *8*, 26622-26629.
25. Yue, Y.; Huo, F.; Ning, P.; Zhang, Y.; Chao, J.; Meng, X.; Yin, C., Dual-site fluorescent probe for visualizing the metabolism of cys in living cells. *J. Am. Chem. Soc.* **2017**, *139*, 3181-3185.
26. Lei, Z.; Li, X.; Luo, X.; He, H.; Zheng, J.; Qian, X.; Yang, Y., Bright, stable, and biocompatible organic fluorophores absorbing/emitting in the deep near-infrared spectral region. *Angew. Chem. Int. Ed.* **2017**, *129*, 3025-3029.
27. Chen, S.; Wang, H.; Hong, Y.; Tang, B. Z., Fabrication of fluorescent nanoparticles based on AIE luminogens (AIE dots) and their applications in bioimaging. *Mater. Horiz.* **2016**, *3*, 283-293.
28. Asanuma, D.; Sakabe, M.; Kamiya, M.; Yamamoto, K.; Hiratake, J.; Ogawa, M.; Kosaka, N.; Choyke, P. L.; Nagano, T.; Kobayashi, H.; Urano, Y., Sensitive β -galactosidase-targeting fluorescence probe for visualizing small peritoneal metastatic tumours in vivo. *Nat. Commun.* **2015**, *6*, 6463.
29. Sharma, A.; Lee, M.-G.; Won, M.; Koo, S.; Arambula, J. F.; Sessler, J. L.; Chi, S. G.; Kim, J. S. Targeting heterogeneous tumors using a multifunctional molecular prodrug. *J. Am. Chem. Soc.* **2019**, *141*, 15611-15618.
30. Yao, Q.; Li, H.; Xian, L.; Xu, F.; Xia, J.; Fan, J.; Du, J.; Wang, J.; Peng, X., Differentiating RNA from DNA by a molecular fluorescent probe based on the "door-bolt" mechanism biomaterials. *Biomaterials* **2018**, *177*, 78-87.
31. Zeng, M.; Shao, A.; Li, H.; Tang, Y.; Li, Q.; Guo, Z.; Wu, C.; Cheng, Y.; Tian, H.; Zhu, W.-H., Peptide receptor-targeted fluorescent probe: visualization and discrimination between chronic and acute ulcerative colitis. *ACS Appl. Mater. Interfaces* **2017**, *9*, 13029-13036.
32. Zhang, H.; Fan, J.; Wang, J.; Dou, B.; Zhou, F.; Cao, J.; Qu, J.; Cao, Z.; Zhao, W.; Peng, X., Fluorescence discrimination of cancer from inflammation by molecular response to COX-2 enzymes. *J. Am. Chem. Soc.* **2013**, *135*, 17469-17475.
33. Li, L.; Shi, W.; Wang, Z.; Gong, Q.; Ma, H., Sensitive fluorescence probe with long analytical wavelengths for γ -glutamyl transpeptidase detection in human serum and living cells. *Anal. Chem.* **2015**, *87*, 8353-8359.
34. Wang, F.; Zhu, Y.; Zhou, L.; Pan, L.; Cui, Z.; Fei, Q.; Luo, S.; Pan, D.; Huang, Q.; Wang, R.; Zhao, C.; Tian, H.; Fan, C., Fluorescent in-situ targeting probes for rapid imaging of ovarian-cancer-specific γ -glutamyltranspeptidase. *Angew. Chem. Int. Ed.* **2015**, *54*, 7349-7353.
35. Chen, Z.; Li, B.; Xie, X.; Zeng, F.; Wu, S., A sequential enzyme-activated and light-triggered pro-prodrug nanosystem for cancer detection and therapy. *J. Mater. Chem. B* **2018**, *6*, 2547-2556.
36. Cheng, P.; Miao, Q.; Li, J.; Huang, J.; Xie, C.; Pu, K., Unimolecular chem-fluoro-luminescent reporter for crosstalk-free duplex imaging of hepatotoxicity. *J. Am. Chem. Soc.* **2019**, *141*, 10581-10584.
37. Kim, D.; Baik, S. H.; Kang, S.; Cho, S. W.; Bae, J.; Cha, M. Y.; Sailor, M. J.; Mook-Jung, I.; Ahn, K. H. Close correlation of monoamine oxidase activity with progress of Alzheimer's disease in mice, observed by in vivo two-photon imaging. *ACS Cent. Sci.* **2016**, *2*, 967-975.
38. He, X.; Xu, Y.; Shi, W.; Ma, H., Ultrasensitive detection of aminopeptidase N activity in urine and cells with a ratiometric fluorescence probe. *Anal. Chem.* **2017**, *89*, 3217-3221.
39. Gu, K.; Xu, Y.; Li, H.; Guo, Z.; Zhu, S.; Zhu, S.; Shi, P.; James, T. D.; Tian, H.; Zhu, W. H., Real-time tracking and in vivo visualization of beta-galactosidase activity in colorectal

- tumor with a ratiometric near-infrared fluorescent probe. *J. Am. Chem. Soc.* **2016**, *138*, 5334-40.
40. Lee, M. H.; Sharma, A.; Chang, M. J.; Lee, J.; Son, S.; Sessler, J. L.; Kang, C.; Kim, J. S., Fluorogenic reaction-based prodrug conjugates as targeted cancer theranostics. *Chem. Soc. Rev.* **2018**, *47*, 28-52.
41. Li, Y.; Xie, X.; Yang, X. e.; Li, M.; Jiao, X.; Sun, Y.; Wang, X.; Tang, B., Two-photon fluorescent probe for revealing drug-induced hepatotoxicity via mapping fluctuation of peroxynitrite. *Chem. Sci.* **2017**, *8*, 4006-4011.
42. Mao, Z.; Feng, W.; Li, Z.; Zeng, L.; Lv, W.; Liu, Z., NIR in, far-red out: developing a two-photon fluorescent probe for tracking nitric oxide in deep tissue. *Chem. Sci.* **2016**, *7*, 5230-5235.
43. Cheng, D.; Peng, J.; Lv, Y.; Su, D.; Liu, D.; Chen, M.; Yuan, L.; Zhang, X., De novo design of chemical stability near-infrared molecular probes for high-fidelity hepatotoxicity evaluation in vivo. *J. Am. Chem. Soc.* **2019**, *141*, 6352-6361.
44. Wang, P.; Zhang, C.; Liu, H.-W.; Xiong, M.; Yin, S.-Y.; Yang, Y.; Hu, X.-X.; Yin, X.; Zhang, X.-B.; Tan, W., Supramolecular assembly affording a ratiometric two-photon fluorescent nanoprobe for quantitative detection and bioimaging. *Chem. Sci.* **2017**, *8*, 8214-8220.
45. Miao, Q.; Yeo, D. C.; Wiraja, C.; Zhang, J.; Ning, X.; Xu, C.; Pu, K., Near-infrared fluorescent molecular probe for sensitive imaging of keloid. *Angew. Chem. Int. Ed.* **2018**, *57*, 1256-1260.
46. Fu, W.; Yan, C.; Guo, Z.; Zhang, J.; Zhang, H.; Tian, H.; Zhu, W.-H., Rational design of near-infrared AIE-active probes: in situ mapping of amyloid- β plaques with ultra-sensitivity and high-fidelity. *J. Am. Chem. Soc.* **2019**, *141*, 3171-3177.
47. Liu, H.-W.; Hu, X.-X.; Li, K.; Liu, Y.; Rong, Q.; Zhu, L.; Yuan, L.; Qu, F.-L.; Zhang, X.-B.; Tan, W., A mitochondrial-targeted prodrug for NIR imaging guided and synergetic NIR photodynamic-chemo cancer therapy. *Chem. Sci.* **2017**, *8*, 7689-7695.
48. Ning, J.; Liu, T.; Dong, P.; Wang, W.; Ge, G.; Wang, B.; Yu, Z.; Shi, L.; Tian, X.; Huo, X.; Feng, L.; Wang, C.; Sun, C.; Cui, J.; James, T. D.; Ma, X., Molecular design strategy to construct the near-infrared fluorescent probe for selectively sensing human cytochrome P450 2J2. *J. Am. Chem. Soc.* **2018**, *141*, 1126-1134.
49. Li, H.; Yao, Q.; Fan, J.; Du, J.; Wang, J.; Peng, X., A two-photon NIR-to-NIR fluorescent probe for imaging hydrogen peroxide in living cells. *Biosens. Bioelectron.* **2017**, *94*, 536-543.
50. Osako, T.; Nishimura, R.; Nishiyama, Y.; Okumura, Y.; Tashima, R.; Nakano, M.; Fujisue, M.; Toyozumi, Y.; Arima, N., Efficacy of intraoperative entire-circumferential frozen section analysis of lumpectomy margins during breast-conserving surgery for breast cancer. *Int. J. Clin. Oncol.* **2015**, *20*, 1093-1101.
51. Kawatani, M.; Yamamoto, K.; Yamada, D.; Kamiya, M.; Miyakawa, J.; Miyama, Y.; Kojima, R.; Morikawa, T.; Kume, H.; Urano, Y., Fluorescence detection of prostate cancer by an activatable fluorescence probe for PSMA carboxypeptidase activity. *J. Am. Soc. Chem.*, **2019**, *141*, 10409-10416.
52. Li, H.; Li, Y.; Yao, Q.; Fan, J.; Sun, W.; Long, S.; Shao, K.; Du, J.; Wang, J.; Peng, X., In situ imaging of aminopeptidase N activity in hepatocellular carcinoma: a migration model for tumour using an activatable two-photon NIR fluorescent probe. *Chem. Sci.*, **2019**, *10*, 1619-1625.
53. Yadav, A. K.; Reinhardt, C. J.; Arango, A. S.; Huff, H. C.; Dong, L.; Malkowski, M. G.; Das, A.; Tajkhorshid, E.; Chan, J., An activity-based sensing approach for the detection of cyclooxygenase-2 in live cells. *Angew. Chem.*, **2020**, *132*, 3333-3340.
54. Shim, J. S.; Kim, J. H.; Cho, H. Y.; Yum, Y. N.; Kim, S. H.; Park, H.-J.; Shim, B. S.; Choi, S. H.; Kwon, H. J., Irreversible inhibition of CD13/aminopeptidase N by the antiangiogenic agent curcumin. *Chem. Biol.* **2003**, *10*, 695-704.
55. Aozuka, Y.; Koizumi, K.; Saitoh, Y.; Ueda, Y.; Sakurai, H.; Saiki, I., Anti-tumor angiogenesis effect of aminopeptidase inhibitor bestatin against B16-BL6 melanoma cells orthotopically implanted into syngeneic mice. *Cancer Lett.* **2004**, *216*, 35-42.
56. He, X.; Hu, Y.; Shi, W.; Li, X.; Ma, H., Design, synthesis and application of a near-infrared fluorescent probe for in vivo imaging of aminopeptidase N. *Chem. Commun.*, **2017**, *53*, 9438-9441.
57. Saiki, I.; Yoneda, J.; Azuma, I.; Fujii, H.; Abe, F.; Nakajima, M.; Tsuruo, T., Role of aminopeptidase N (CD13) in tumor-cell invasion and extracellular matrix degradation. *Int. J. Cancer* **1993**, *54*, 137-143.
58. Mina-Osorio, P., The moonlighting enzyme CD13: old and new functions to target. *Trends Mol. Med.* **2008**, *14*, 361-371.
59. Li, H.; Yao, Q.; Xu, F.; Xu, N.; Duan, R.; Long, S.; Fan, J.; Du, J.; Wang, J.; Peng, X., Imaging γ -Glutamyltranspeptidase for tumor identification and resection guidance via enzyme-triggered fluorescent probe. *Biomaterials* **2018**, *179*, 1-14.
60. Gennari, L.; Doci, R.; Bignami, P.; Bozzetti, F., Surgical treatment of hepatic metastases from colorectal cancer. *Ann. Surg.* **1986**, *203*, 49-54.
61. Gennar, L.; Doci, R.; Bozzetti, F.; Veronesi, U., Proposal for a clinical classification of liver metastases. *Tumori J.* **1982**, *68*, 443-449.

Entry for the Table of Content (TOC)

